


Effect of Bubbles Produced from Hydrate-Bearing Particle Dissociation on Particle Motion in Water

Peng Li, Danning Liu, Xuhui Zhang,* and Xiaobing Lu

 Cite This: *Energy Fuels* 2021, 35, 1371–1380

 Read Online

ACCESS |

 Metrics & More

 Article Recommendations

ABSTRACT: Understanding the motion of natural gas hydrate-bearing particles in a pipeline is of great significance for developing natural gas exploitation technology. In this study, the effect of bubbles produced from hydrate dissociation on the particle settling characteristics and the drag coefficient were studied under different Reynolds numbers. In the experiment, two types of porous solid spherical particles, namely, silty clay and quartz, were used to study the settling of ordinary particles and hydrate-bearing particles using a customized experimental apparatus. The settling and dissociation of the particle in water and the motion of bubbles were captured using a high-speed camera. The results showed that the gas from the hydrate dissociation surrounded the particle, which caused the boundary layer at the particle surface to prematurely separate at the back end of the particle, thereby increasing the interaction forces between the particle and the water during motion. The influence of bubbles on the particle motion was closely related to the hydrate dissociation rate and the particle settling velocity. Moreover, a mathematical expression is provided to describe the entire process from sediment particles entering the water to hydrate dissociation. Furthermore, the dissociation rate of the hydrate-bearing sediment particle under water flow was obtained.

1. INTRODUCTION

Natural gas hydrate has become a very important strategic energy source in China as a result of its large reserves and low pollution. Countries around the world have accelerated the exploitation and development of natural gas hydrate.¹ Trial production of hydrates has demonstrated that current hydrate exploitation methods (thermal stimulation method, depressurization method, CO₂-replacement method, and chemical injection method) can dissociate gas hydrate through the interference of the temperature and pressure. However, these methods are challenging to meet the development efficiency requirements of commercial development.^{2,3} Zhang and Lu⁴ proposed a new method called mechanical–thermal exploitation, considering the low heat transfer and mining efficiency of the traditional exploitation methods. The details of the method can be found in the literature. The first step of mechanical–thermal exploitation is to excavate the hydrate formation like coal mining. The resulting sediments are cut into small particles, which are then mixed with the warmer seawater and transported through a vertical pipe to the storage tank on the surface of the sea. In the uplift process, gas hydrate dissociates with the decrease of the pressure and the increase of the temperature and the soil is separated and backfilled. The transportation of marine natural gas hydrate-bearing sediment via a pipeline is a fundamental problem in realizing the development and utilization of hydrate resources.

During the transportation process, the complex gas–liquid–solid three-phase flow accompanied by hydrate dissociation appears in the pipeline, significantly different from the general gas–liquid–solid three-phase transportation pipeline flow.⁵ During the upward transport of a sediment particle and seawater mixture, the hydrate is dissociated to produce gas.

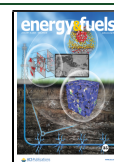
Multiphase flow and hydrate dissociation occur simultaneously and interact, creating a highly non-equilibrium multiphase flow problem involving heat and mass transfer. The hydrate dissociation changes the state parameters, such as the temperature, pressure, and concentration of each phase in the pipeline. The water temperature, flow velocity, and particle size affect the dissociation rate of hydrate-bearing particles in the flow process. It is of great significance to fully understand the dissociation and flow behaviors of hydrate-bearing particles under flow conditions. The gas–liquid–solid flow involving the hydrate dissociation is a new problem in hydrate exploitation. Only preliminary studies are reported on it.⁶

Wang⁷ proposed a model to calculate the annular multiphase flow involving phase transition of natural gas hydrate. The hydrate dissociation was considered by adding source terms to the mass, momentum, and energy conservation equations. Wei et al.⁸ used the same method to calculate the multiphase flow of hydrate-bearing particles with drilling fluid during the drilling of deepwater natural gas hydrate. However, interphase forces and heat exchange between phases were not considered in the model, and the solid particles were assumed to be pure methane hydrate-bearing particles. On the basis of engineering experience involving the cutter suction exploitation of submarine natural gas hydrate, Xu et al.⁹ calculated the

Received: November 7, 2020

Revised: December 23, 2020

Published: January 5, 2021



dissociation characteristics of a hydrate in hydraulic lifting pipelines and the influence of the flow parameter change on the dissociation using an established mathematical model, and they obtained the changes of the temperature, pressure, and hydrate-bearing particle dissociation rate and amount over the whole flow process. The model accounted for the heat exchange between seawater and a pipeline, not accounting for the heat transfer between phases. The temperature, pressure, and velocity fields were calculated separately, and the coupling relationship between the hydrate dissociation and multiphase flow was not considered. In addition, the influence of gas–liquid–solid three-phase interphase forces on the velocity field was not considered in the model. On the basis of engineering experience involving deepsea shallow natural gas hydrate solid-state fluid mining, Tang¹⁰ studied the pipeline transport characteristics of a natural gas hydrate slurry. The hydrate dissociation and multiphase flow were coupled using a source term in the conservation equation. The Kim–Bishnoi dissociation model was used as the hydrate dissociation model. The interaction between the hydrate dissociation and the multiphase flow was calculated by considering the interphase forces between the phases, while the heat exchange between the phases was not considered. Similarly, solid particles were pure methane hydrate-bearing particles.

Currently, most of the hydrate dissociation models under pipeline flow conditions are based on a statistical analysis of macroscopic experimental data, and they do not account for the heat conduction inside the particles or the evolution of the hydrate dissociation process.¹¹ Furthermore, the bubbles that flow out of the solid particles attach to the surfaces of particles and have a significant impact on the movement of the particles in water. In previous studies, the multiphase flow in the hydrate-bearing sediments was generally treated to the gas and water flow as a result of the sediment skeleton assumed to be stagnant.¹² Gas hydrate is part of the sediment skeleton, and the hydrate dissociation changes the structure of pores in sediments and the flow path of gas and water.^{13–15} A multitude of studies have conducted the absolute permeability,¹⁶ the gas–water relative permeability,¹⁷ the relationship of the capillary pressure to the saturations of the fluid phase,¹⁸ and the gas and water flow in the hydrate-bearing sediments.¹² However, the understanding of the interaction between the gas bubbles and the hydrate-bearing sediment particles is insufficient. In this study, we mainly focus on the effect of the bubbles on the particle motion, and the migration process of gas and water in the particle is out of the scope of this paper and will not be discussed here.

When a mixture of hydrate-bearing particles and seawater is continuously transported, the migration distance of the solid particles from the beginning of the hydrate dissociation in the pipeline to the complete dissociation is defined as the dissociation equilibrium height. In the mechanical–thermal combined mining method, the dissociation equilibrium height determines the installation position of the separation system. Li et al.¹⁹ obtained a power relationship of the dissociation equilibrium height using numerical simulation and then obtained a simplified expression of the dissociation equilibrium height using a dimensional analysis method. The theoretically predicted values were in good agreement with the numerically simulated results within a certain range of dimensionless parameters. However, how produced bubbles affect the particle motion was not well-understood. In actual pipeline transport, the hydrate dissociation causes the flow in the pipeline to

change from a solid–liquid two-phase flow to a gas–liquid–solid three-phase flow. The introduction of gas affects the degree of turbulence in the water flow and the forces between the particles and the water, thereby changing the dissociation equilibrium height of the hydrate-bearing particles.

Studies on the influence of bubbles on the particle motion mainly focus on the drag reduction effect.²⁰ A thin gas layer is formed on the surface of the particle by artificially injecting tiny bubbles or making cavitation bubbles.²¹ Using a high-speed camera, Vakarelski et al.²² found that, after a high-temperature metal ball fell into the water, Leidenfrost vapor layers formed on the surface of the ball, which could reduce the fluid drag by up to 85%. The mechanism of drag reduction was as follows: On the one hand, the low-density and low-viscosity gas layer around the ball caused the solid–liquid boundary condition to change from no-slip boundary conditions to partial- or full-slip boundary conditions, which reduced the friction drag of the surface. On the other hand, the generation of gas delayed the separation of the boundary layer, thereby reducing the pressure drag of the particle motion. When hydrate-bearing particles dissociated, gas was generated from inside of the particles and glided along the surfaces of the particles under the action of buoyancy until separating from the particles. This process is different from that when gas is introduced artificially, and thus, a new experimental study is necessary.

In this study, we obtained a thermal dissociation evolutionary model of a single hydrate-bearing sediment particle in water using both experimental and theoretical studies to clarify the influence of gas bubbles from hydrate dissociation on the particle motion. The study provides the necessary parameters for multiphase transport analysis of hydrate-bearing sediment particles in a pipeline and can be used for the design, operation, and management of deepwater natural gas hydrate transportation pipelines. Section 2 describes the experimental setup. Experimental phenomena and results are presented in section 3, and section 4 discussed the reasons for the settling velocity of the non-hydrate particle being higher than that of the hydrate-bearing particle.

2. EXPERIMENTAL SECTION

2.1. Generation of Hydrate-Bearing Particles. Seabed silt clay from the Shenhu area in the South China Sea and artificially prepared quartz balls supplied by EHEIM SUBSTRATpro were selected as the sediment skeleton for hydrate synthesis. Seabed sediment soil was mixed with distilled water to form soil samples with a moisture content of 22%. Then, spherical particles with diameters of 6–8 mm were prepared using a silica gel spherical mold. The porosities of the spherical clay particles were about 0.4. The diameters of the artificially prepared quartz ball were 8 mm, and their porosities were about 0.45. Before hydrate formation, the quartz ball particles were immersed in water and stirred sufficiently to fill the pores of the particles with water. The whole synthesis device of hydrate-bearing sediment particles consisted of four parts: an autoclave, gas tank, gas compressor, and temperature control box, as shown in Figure 1. The temperature control box could provide a temperature between 243 and 303 K (with an accuracy of 0.5 K). The autoclave was made of stainless steel, with an inner diameter of 7.5 cm, a height of 30 cm, and a maximum pressure of 30 MPa, and its internal capacity could be altered using a moving piston. The main function of the gas compressor was to provide the gas and maintain the gas pressure required for the synthesis of hydrates. The gas tank was used to store the gas required for hydrate synthesis. Under laboratory conditions, hydrates are more easily generated from carbon dioxide gas than methane gas. Although the dissociation rate between carbon dioxide

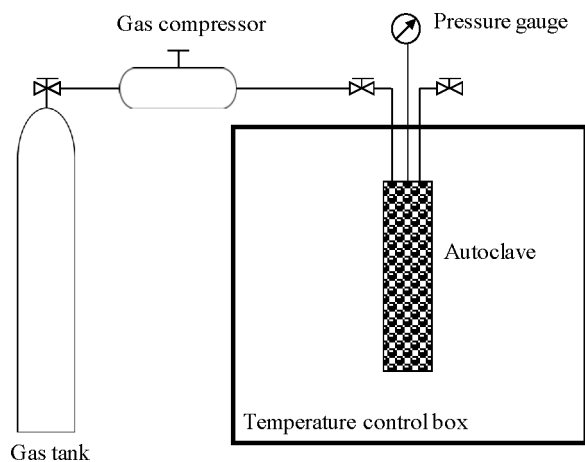


Figure 1. Experimental apparatus for the synthesis of hydrate-bearing sediment particles.

hydrate and methane gas hydrate is different under the same temperature and pressure, the thermodynamic and mechanical parameters of carbon dioxide hydrate and methane hydrate are similar. Thus, carbon dioxide hydrate was used as a substitute for methane hydrate in this study considering the operability, safety, and cost of the experiment.²³

First, the temperature of the control box was set to 268 K, which remained unchanged during the hydrate synthesis process. Carbon dioxide gas was introduced into the autoclave using a gas compressor, and the gas pressure was set at 5 MPa. The hydrate phase equilibrium temperature is obtained by the phase equilibrium condition of carbon dioxide hydrate proposed by Sloan²⁴

$$P_e = 10^{-3} \exp\left(\alpha + \frac{\beta}{T_e}\right) \quad (1)$$

where $\alpha = 44.6$, $\beta = -1.02 \times 10^4$, T_e is the phase equilibrium temperature (K), and P_e is the phase equilibrium pressure (MPa).

In the process of hydrate synthesis, the autoclave was an isovolumetric system. The synthesis process lasted about 48–72 h until the autoclave pressure no longer changed with time. After the synthesis, the inlet pressure of the autoclave was adjusted using a pressure-regulating valve to reduce the pressure in the autoclave to 0.1 MPa, i.e., to maintain a balance with the atmospheric pressure. Next, the temperature of the control box was further reduced to 253 K for 3–4 h. Finally, spherical sediment particles containing hydrate were obtained, as shown in Figure 2.

2.2. Measurement of Saturation of Hydrate Samples. The procedure for measuring the hydrate saturation in the spherical hydrate-bearing sediment particles was as follows:²³ A container with

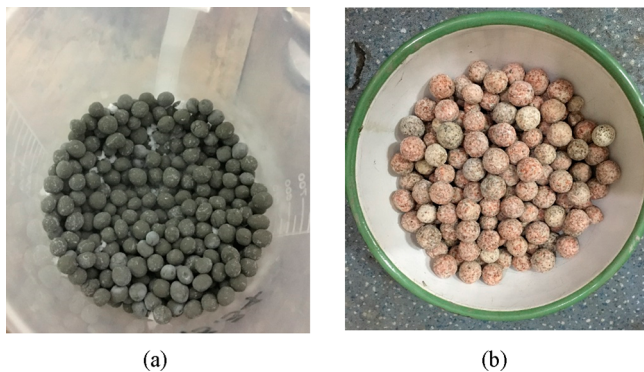


Figure 2. Hydrate-bearing (a) silty clay and (b) quartz particles prepared in the laboratory.

a good seal was weighed to determine its mass m_0 . A single hydrate-bearing particle was removed from the autoclave and inserted into the container. A NewClassic ME electronic balance (with an accuracy of ± 0.0001 g) was used to weigh the total mass of the container and the particle m_1 . The container was placed in a room-temperature environment until the hydrate in the particle completely dissociated. After the carbon dioxide gas was released from the dissociation process, the total mass of the container m_2 was determined by weighing. The dissociated particle was placed in a drying oven at 373.15 K for 12 h. The total mass of the particle and the container m_3 was determined by weighing after complete drying.

The hydrate saturation was defined as the ratio of the volume of the hydrate in the pores to the total volume of the pores

$$S_h = \frac{V_h}{V_a + V_w + V_h} \quad (2)$$

where the hydrate volume $V_h = m_{CO_2} M_h / M_{CO_2} \rho_h$, where m_{CO_2} represents the mass of carbon dioxide gas that forms a hydrate in a single particle, with $m_{CO_2} = m_1 - m_2$, and the density ρ_h of carbon dioxide hydrate was set to 1117 kg/m³,²⁵ and the water volume $V_w = m_w / \rho_w$ where m_w is the mass of water in a single hydrate-bearing particle, with $m_w = m_2 - m_3 - 5.75 m_{CO_2} M_{H_2O} / M_{CO_2}$, and the density ρ_w of water was set to 998.2 kg/m³. Therefore, the volume of air in a single particle V_a can be expressed as follows:

$$V_a = \frac{\phi}{1 - \phi} V_{sand} - V_w - V_h \quad (3)$$

where ϕ is the porosity and $V_{sand} = m_{sand} / \rho_{sand}$, where m_{sand} represents the mass of the soil skeleton in a single particle, with $m_{sand} = m_3 - m_0$. It is noted that the uncertainty of the hydrate saturation may derive from the following aspects: (i) the hydrate content in different particles produced in the same batch may be heterogeneously distributed, and (ii) the particle porosity measured before hydrate formation may change during hydrate synthesis.

After hydrate saturation was achieved, the density of the spherical hydrate-bearing particle could be obtained by dividing the total mass of the particle by the total volume of the particle

$$\rho_p = \frac{m_p}{V_p} = \frac{m_{sand} + m_w + m_h + m_a}{V_{sand} + V_w + V_h + V_a} \quad (4)$$

where m_h represents the mass of gas hydrate, with $m_h = \rho_h V_h$, and m_a represents the mass of air, with $m_a = \rho_a V_a$, where $\rho_a = 1.225$ kg/m³.

2.3. Dissociation of a Single Spherical Hydrate-Bearing Sediment Particle. A dissociation experiment of a single spherical hydrate-bearing sediment particle was carried out under atmospheric pressure. The particle fell freely from a height of 3–5 cm over the water surface. The dissociation phenomenon of the particle in the process of falling in the water was observed. The water temperature range was 273.15–298.15 K. The hydrate dissociation was driven by the temperature difference between the water and the particle. When the temperature of the external surface of the particle exceeded the phase equilibrium temperature of the hydrate, the hydrate began to dissociate and produce gas. The particle motion and hydrate dissociation were recorded using a high-speed camera [Phantom VEO410L with direct current (DC) power and light-emitting diode (LED) lighting] at a frequency of 5200 frames per second.

In this study, the change of the drag coefficient C_D was used to measure the influence of the bubbles produced from the hydrate dissociation on the particle motion. During the falling process of the spherical particle in the liquid, when the gravitational, buoyancy, and drag forces acting on the particle reached equilibrium, the drag coefficient could be defined using the ultimate settling velocity u_t of the particle

$$C_D = \frac{4(\rho_p - \rho_w)d_p g}{3\rho_w u_t^2} \quad (5)$$

where ρ_p is the density of the particle, d_p is the diameter of the particle, and g is the acceleration of gravity.

The particle Reynolds number was defined as follows:

$$Re = \frac{\rho_w d_p u_t}{\mu_w} \quad (6)$$

where μ_w is the viscosity of the water.

To study the dependence of the drag coefficient upon the Reynolds number, five groups of experiments were performed on the hydrate-bearing and non-hydrate particles with different materials and particle sizes. The range of the particle Reynolds number was $2039 \leq Re \leq 3346$. To eliminate the experimental error, each group of experiments was repeated at least 3 times, and the average value was taken. The details of the experimental schemes are shown in Table 1. In all of the experimental schemes, the water temperature was 283.15 K and the initial particle temperature was 253.15 K.

Table 1. Experimental Scheme of Hydrate-Bearing Particle Settling

| type | material | density (kg/m ³) | diameter (mm) | Re | C _D |
|---------------------------|------------|------------------------------|---------------|------|----------------|
| hydrate-bearing particles | quartz | 1806 | 8 | 2957 | 0.618 |
| | silty clay | 2069 | 6 | 2179 | 0.640 |
| | silty clay | 2076 | 7 | 2656 | 0.573 |
| | silty clay | 2108 | 8 | 3250 | 0.610 |
| ordinary particles | quartz | 1719 | 8 | 2770 | 0.629 |
| | silty clay | 1686 | 6 | 2039 | 0.481 |
| | silty clay | 2065 | 6 | 2468 | 0.500 |
| | silty clay | 2077 | 8 | 3346 | 0.560 |
| | glass | 2600 | 6 | 2949 | 0.519 |
| | quartz | 1654 | 8 | 2913 | 0.518 |

3. RESULTS

When the hydrate-bearing particle fell in the water, convective heat transfer occurred between the particle surface and the surrounding water with a higher temperature. When the temperature of the particle surface layer reached the phase equilibrium temperature of the hydrate, the hydrate in the pores of the particle dissociated to produce gas and the gas flowed out of the particle pores to form a large number of bubbles surrounding the particle. The bubbles from the hydrate dissociation completely covered the entire surface of the particle. They can be thought of forming a low-density and low-viscosity gas layer around the particle. Driven by buoyancy, the bubbles at the front end of the particle slid upward along the particle surface, separated from the particle at a particular position at the back end of the particle, and continued to move upward. With the dissociation of hydrate, the large number of generated bubbles formed a long trail at the back end of the particle as the particle fell through the water. The experimental phenomena are shown in Figure 3. The porosity and pore size of the quartz ball were larger than that of the clay ball, and more hydrate could be synthesized in the quartz balls. When falling in water, the dissociation process of the hydrate-bearing quartz ball was more rapid than that of the hydrate-bearing clay ball. For the silt clay particle, surface soil grains (at sizes from several micrometers to tens of micrometers) were separated from the hydrate-bearing particle

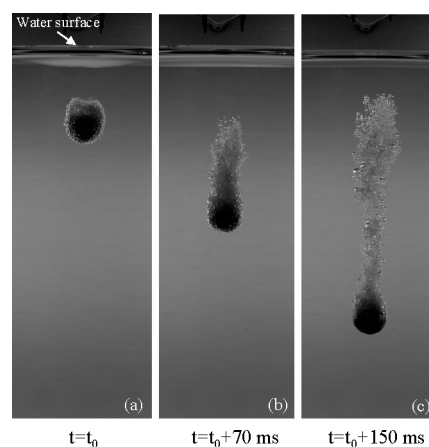


Figure 3. Dissociation of a single spherical hydrate-bearing particle in water.

as a result of the great decrease in the cohesion between the soil grains after the dissociation of hydrate took place. The breakage of the particle during the hydrate dissociation process is not apparent before the particle reaches the ultimate settling velocity. The breakage process is not considered in this paper. The quartz particle was not broken during the hydrate dissociation.

Figure 4 shows the difference in the settling velocity between the hydrate-bearing and non-hydrate clay particles produced in

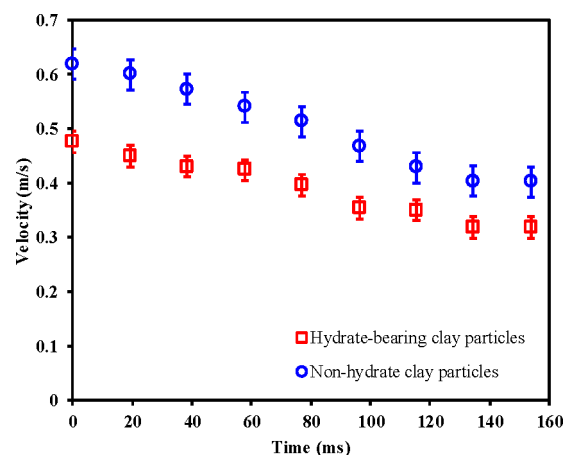


Figure 4. Variation of the settling velocity of hydrate-bearing and non-hydrate clay particles falling in the water. The red box highlights hydrate-bearing particles, while the blue circle highlights non-hydrate particles. The upper and lower limits of the error line were obtained on the basis of the standard deviation of the ultimate settling velocity obtained in repeated falling experiments.

the same batch (i.e., the porosity and moisture content were consistent). The two particles had the same diameter and fell from the same position on the water surface. The starting point for the timing was the position where the particle fell one particle diameter into the water. The data showed that the settling velocity of the two kinds of particles gradually decreased before reaching a stable level. When the settling velocity was constant, the force on the particles had reached a steady status of the mechanical equilibrium. Upon entering the water, the settling velocity of the non-hydrate particle was higher than that of the hydrate-bearing particle. When the velocity reached equilibrium, the ultimate settling velocity of

the hydrate-bearing particle was 0.79 times that of the non-hydrate particle, corresponding to a 9% increase in the drag effect. Because the hydrate content in a single particle was limited, after a sufficiently long time, the number of the bubbles on the particle surface continually decreased in the later stage of dissociation and the influence of bubbles on particle motion could be ignored. If the crushing effect of the particle were not considered, the ultimate settling velocity of the hydrate-bearing particle would approach that of the non-hydrate particle.

To study the dependence of the drag coefficient upon the Reynolds number in the falling process of the particles, comparative experiments were carried out using hydrate-bearing and non-hydrate particles with different materials and diameters, of which the results are shown in Figure 5. The non-

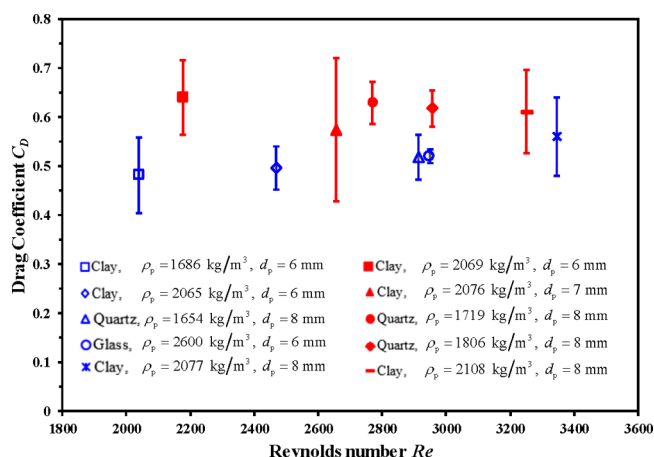


Figure 5. Variation of the drag coefficient with Reynolds number for hydrate-bearing and non-hydrate particles. The blue symbols correspond to the non-hydrate particles, and the red symbols correspond to the hydrate-bearing particles. The error line was obtained by adding and subtracting the standard deviation from the average of multiple repeated experiments.

hydrate particles included clay particles, quartz balls, and glass beads prepared in the laboratory. The hydrate-bearing particles were prepared using clay particles and quartz balls. In the Reynolds number range of $2039 \leq Re \leq 3346$, the drag coefficient C_D of the two types of particles did not change significantly. The variation range of the drag coefficient of the hydrate-bearing particle was $0.573 \leq C_D \leq 0.640$, and that of the non-hydrate particle was $0.481 \leq C_D \leq 0.560$. Generally, in the Reynolds number range of this experiment, the gas from the hydrate dissociation surrounded the particle, which increased the interaction force between the particle and the water when the particle moved in the water. When the water was still, it increased the drag during the particle motion.

4. DISCUSSION

The effect of the bubbles on the particle motion mainly involved two mechanisms: (1) the bubbles created a low-density and low-viscosity gas layer around the particle, which changed the no-slip boundary condition at the solid–liquid boundary and reduced the friction drag of the surface, and (2) the disturbance effect of the bubbles from the dissociation on the boundary layer increased the formation drag caused by the pressure difference between the front and back of the particle. The effect of changing the no-slip boundary condition could be

measured using the ratio of the effective slip length λ_s to the thickness λ_B of the viscous boundary layer: $\lambda_s/\lambda_B \sim |dr_p/dt|/u_t$. The effective slip length was defined as the extrapolated thickness with zero velocity at the particle surface, and r_p represents the radius of the hydrate area. $|dr_p/dt|$ represents the dissociation rate of the hydrate and was considered to be the increased rate of boundary layer thickness when the fluid flowed past the particle surface.²⁶ The disturbance of the bubbles on the boundary layer could be measured using the ratio of the initial bubble size d_b formed when the gas exited the pores of the particle to the thickness λ_B of the viscous boundary layer. For the motion of a spherical particle in water, the characteristic thickness of the boundary layer could be measured using $2.74d_p/\sqrt{Re}$.²⁷ The maximum diameters of the bubbles formed when gas flowed out of the pores of the particle were closely related to the dissociation rate of the hydrate and the settling velocity of the particle. Therefore, the dissociation rate of the hydrate was important for both physical processes.

4.1. Dissociation Rate of Hydrate under Convective Heat Transfer Conditions. It was assumed that an ideal spherical hydrate-bearing particle fell in still water, and the particle contained three components: hydrate, water, and a sediment skeleton. The pores of the particle were completely filled with hydrate and water. In addition, the breakage of the particle during the hydrate dissociation process was not taken into account, and the temperature of the surrounding water was higher than that of the particle. Because the latent heat of the hydrate dissociation had a large order of magnitude, the latent heat absorbed in the dissociation process of the hydrate was far greater than the increased sensible heat. Therefore, the dissociation region of the hydrate was separated from the undissociated region by a distinct interface rather than a large transition region. On this basis, it was assumed that the hydrate-bearing particle was composed of a dissociation region (1) and an undissociated region (2) during the dissociation process, as shown in Figure 6. The temperature of the

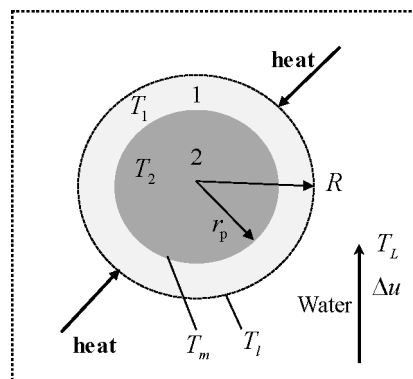


Figure 6. Hydrate dissociation process of the hydrate-bearing particle falling in the water. The dark gray region in the center is the undissociated region, and the peripheral light-colored region is the dissociation region.

outermost layer of the dissociation region was T_1 ; the interface temperature was the phase equilibrium temperature T_m of the hydrate; the temperature of the surrounding water was T_w ; the initial radius of the particle was R ; the radius of the hydrate region was r_p ; and the velocity difference between the particle and water was Δu .

Considering the two physical effects of heat conduction and hydrate dissociation, the one-dimensional energy equations of hydrate dissociation in the dissociation and undissociated regions were obtained as follows:²⁸

dissociation region

$$c_1 \rho_1 \frac{\partial T_1}{\partial t} = k_1 \frac{\partial^2 T_1}{\partial r^2} \quad (7)$$

initial condition

$$T_1(r, 0) = T_{p0} \quad (8)$$

boundary condition

$$r = R: \quad k_1 \left. \frac{\partial T_1}{\partial r} \right|_{r=R} = h_c [T_L - T_1(R, t)]$$

$$r = r_p: \quad T_1 = T_m \quad (9)$$

undissociated region

$$c_2 \rho_2 \frac{\partial T_2}{\partial t} = k_2 \frac{\partial^2 T_2}{\partial r^2} \quad (10)$$

initial condition

$$T_2(r, 0) = T_{p0} \quad (11)$$

boundary condition

$$r = 0: \quad \left. \frac{\partial T_2}{\partial r} \right|_{r=0} = 0$$

$$r = r_p: \quad T_2 = T_m \quad (12)$$

The subscripts 1 and 2 represent the dissociation region and the undissociated region of the hydrate, respectively. The specific heat c , thermal conductivity coefficient k , and density ρ of each region were taken as the volume averages of each component; ΔH is the latent heat of hydrate dissociation; ε_h is the volume fraction of hydrate in the particle, with $\varepsilon_h = S_h \phi$; and h_c is the convective heat transfer coefficient between the particle and water. If the specific distribution of the internal temperature of the particle is not considered and attention is only paid to the variation of the dissociation interface, the temperature gradient conditions at the dissociation interface can be obtained using $|\mathrm{d}r_p/\mathrm{d}t|$ to measure the dissociation rate of the hydrate, as follows:

$$\rho_h \Delta H \varepsilon_h \frac{\mathrm{d}r_p}{\mathrm{d}t} = k_1 \frac{\partial T_1}{\partial r} - k_2 \frac{\partial T_2}{\partial r} \quad (13)$$

The first term on the right side of the equation represents the temperature gradient in the dissociation region, and the second term represents the temperature gradient in the undissociated region. As per the processing method presented by Bansal and Nikrityuk,²⁹ the thermal conductivity expression of the spherical particle was used to substitute the temperature gradient value. Finally, the hydrate dissociation rate expression was obtained

$$\rho_h \Delta H \varepsilon_h r_p^2 \frac{\mathrm{d}r_p}{\mathrm{d}t} = \frac{k_1 (T_m - T_1)}{1/r_p - 1/R} - \frac{k_2 (T_p - T_m)}{1/r_t - 1/r_p} \quad (14)$$

where $r_t = 0.01R$. The value of T_1 can be obtained by the balance of the convective heat transfer and the heat conduction at the particle–water interface

$$h_c (T_1 - T_L) = \frac{k_1 (T_m - T_1)}{(1/r_p - 1/R) R^2} \quad (15)$$

The convective heat transfer coefficient at the particle surface was calculated as $h_c = Nu k_L / d_p$, where the Nusselt number Nu was calculated using the following expression:

$$Nu = 2.0 + 0.6 Re^{1/2} Pr^{1/3} \quad (16)$$

4.2. Diameters of Detaching Bubbles. The hydrate inside the particle dissociated into gas and flowed to the particle surface through the pores to form bubbles, which periodically detached from the particle surface. The maximum diameter of a detaching bubble depended upon the balance of various forces exerted on the bubble. In this experiment, the bubbles generated at the front end of the particle slid upward along the particle surface driven by buoyancy and merged with other bubbles that formed at other positions, forming larger bubbles. Only the maximum diameters of bubbles detaching at the front end of the particle in the particle falling process were studied, which could represent the minimum thickness of the gas layer around the particle. The forces on the bubble are shown in Figure 7. It was assumed that the bubbles remained

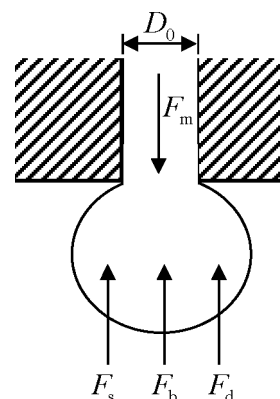


Figure 7. Forces in the bubble detachment process at the front end of the settling particle.

spherical in the process of formation and detachment. The pore width of the particle was D_0 . The forces exerted on a bubble were the gas momentum force, which caused the bubble to detach from the surface, and the forces that caused the bubbles to adhere to the surface, including buoyancy, surface tension, and the drag force as a result of the water flow.

The mathematical expression for each force is as follows:

gas momentum force

$$F_m = \frac{4 \rho_g Q_0^2}{\pi D_0^2} \quad (17)$$

where ρ_g denotes the density of the gas and Q_0 denotes the gas flow exiting the pores. Q_0 can be calculated using the following equation:

$$Q_0 = \frac{4A\pi R^3 \varepsilon_h}{3nt_{\text{dis}}} \quad (18)$$

where $A = 166.8$, which means that 166.8 m^3 of gas can be produced after dissociation of 1 m^3 of carbon dioxide hydrate, n is the number of bubble flow outlets on the particle surface, and t_{dis} is the time from the beginning of hydrate dissociation to the end of dissociation, which can be obtained using eq 11.

buoyancy

$$F_b = \frac{4}{3}\pi r_b^3(\rho_w - \rho_g)g \quad (19)$$

where r_b is the radius of the bubble.

surface tension

$$F_s = \pi D_0 \sigma \quad (20)$$

drag force³⁰

$$F_d = 6\pi\mu_w r_b \left(\frac{dr_b}{dt} + u_t \right) \quad (21)$$

where dr_b/dt represents the expansion rate of the bubble.

The equilibrium force equation of the bubble is

$$\frac{4}{3}\pi r_b^3(\rho_w - \rho_g)g + 6\pi\mu_w r_b \left(\frac{dr_b}{dt} + u_t \right) + \pi D_0 \sigma = \frac{4\rho_g Q_0^2}{\pi D_0^2} \quad (22)$$

and the variation of the bubble radius can be obtained as follows:

$$\frac{dr_b}{dt} = -u_t - \frac{2r_b^2(\rho_w - \rho_g)g}{9\mu_w} + \frac{2\rho_g Q_0^2}{3\pi^2 D_0^2 \mu_w r_b} - \frac{D_0 \sigma}{6\mu_w r_b} \quad (23)$$

The maximum diameter of the bubbles formed on the particle surface at a certain dissociation rate can be obtained using eqs 11 and 20.

4.3. Model Validation and Mechanism Interpretation.

When $T_L = 283.15 \text{ K}$ and $T_{p0} = 283.15 \text{ K}$, for a hydrate-bearing quartz particle with a diameter of 0.008 m and an ultimate settling velocity of 0.35 m/s , $S_h = 70\%$ and $\phi = 0.45$. Through calculation, it was determined that $t_{\text{dis}} = 150 \text{ s}$ and the dissociation rate of the hydrate was $|dr_p/dt| \sim 2.67 \times 10^{-5} \text{ m/s}$. The ratio of the effective slip length to the thickness of the boundary layer was $\lambda_s/\lambda_B \sim 7.62 \times 10^{-5}$. For a hydrate-bearing clay particle, $S_h = 20\%$ and $\phi = 0.40$. Through calculation, it was determined that $t_{\text{dis}} = 40 \text{ s}$, the dissociation rate of the hydrate was $|dr_p/dt| \sim 1 \times 10^{-4} \text{ m/s}$, and $\lambda_s/\lambda_B \sim 2.86 \times 10^{-4}$. The effective slip length was generally 3–4 orders of magnitude smaller than the thickness of the boundary layer. In addition, the reduction in the frictional drag on the particle surface caused by the generated bubbles was relatively small, and this mechanism of action did not play a leading role in this experiment.

Under the above conditions of the water temperature and settling velocity, the maximum diameter d_b of the detaching bubbles was calculated to be 0.4 mm for the hydrate-bearing clay and hydrate-bearing quartz particles, which was close to the results obtained using the high-speed camera in this experiment. On the basis of the experimental images and the calculated diameter of the detaching bubbles, the average number of gas bubbles adhering to the solid particle was calculated to be about 1000. The ratio of the detaching bubble diameter d_b to the viscous boundary layer thickness λ_B was $d_b/\lambda_B \sim d_b\sqrt{Re}/2.74d_p \sim 0.96$. This showed that the bubble

diameter was basically of the same order of magnitude as the thickness of the boundary layer, which indicated that the boundary layer was separated on both sides of the particle as a result of the disturbance of the bubble transport from the hydrate dissociation, thus increasing the pressure drag of the particle motion. The values of the physical parameters used in the above calculation are shown in Table 2.

Table 2. Values of Physical Parameters Used To Calculate the Dissociation Rate and Detaching Bubble Diameter

| physical parameter | value |
|---|-----------|
| Water | |
| density, ρ_w (kg/m^3) | 998.2 |
| thermal conductivity, k_w ($\text{W m}^{-1} \text{K}^{-1}$) | 0.6 |
| specific heat, c_w ($\text{J kg}^{-1} \text{K}^{-1}$) | 4182 |
| viscosity, μ_w (Pa s) | 10^{-3} |
| Hydrate | |
| phase equilibrium temperature, T_m (K) | 257.15 |
| density, ρ_h (kg/m^3) | 1117 |
| thermal conductivity, k_h ($\text{W m}^{-1} \text{K}^{-1}$) | 0.324 |
| Sand | |
| thermal conductivity, k_{sand} ($\text{W m}^{-1} \text{K}^{-1}$) | 3 |
| Carbon Dioxide | |
| thermal conductivity, k_g ($\text{W m}^{-1} \text{K}^{-1}$) | 0.015 |
| density, ρ_g (kg/m^3) | 1.997 |
| surface tension coefficient of the gas–water interface, σ (N/m) | 0.072 |
| Particle | |
| pore width, D_0 (μm) | 1 |
| number of surface gas outlet, n | 100 |

To further verify the accuracy of the above model, a comparative experiment was performed on the dissociation of the hydrate-bearing quartz particle under cold and warm water conditions. Different water temperatures resulted in different dissociation rates of the hydrate. Therefore, the effect of bubbles on the particle motion varied. In the comparative experiment, the particles had the same diameter and hydrate saturation and detached at the same position on the water surface. The cold water temperature was set to 273.15 K , and the warm water temperature was set to 343.15 K . The values of the parameters related to the particles and water are shown in Table 3. Figure 8 shows the change of the settling velocity of

Table 3. Experimental Conditions of Hydrate-Bearing Quartz Ball Falling in Cold and Warm Water

| | |
|--------------------------------------|--|
| water temperature (K) | cold water, 273.15; warm water, 343.15 |
| initial temperature of particles (K) | 253.15 |
| particle diameter (mm) | 8 |
| particle porosity | 0.45 |
| hydrate saturation (%) | 70 |

hydrated-bearing quartz particles produced in the same batch in cold and warm water. With the position where particles fell one particle diameter into the water taken as the starting point for the timing, the settling velocity of the particles in cold water decreased gradually from 0.85 m/s and finally stabilized at 0.29 m/s . In contrast, the settling velocity decreased gradually from 0.84 m/s and finally stabilized at 0.24 m/s in warm water. Thus, the ultimate settling velocity of the hydrate-bearing particles in warm water was smaller than that in cold water. In

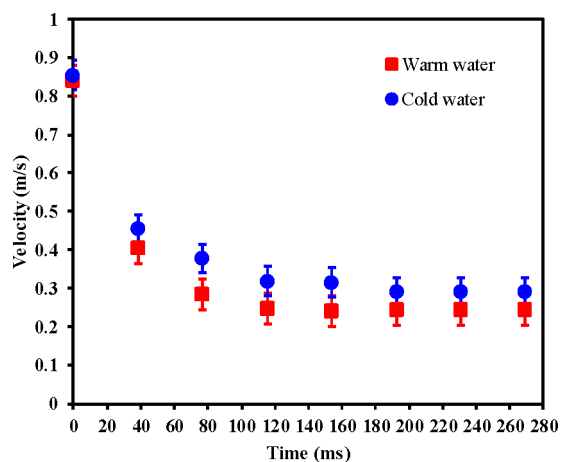


Figure 8. Variations of the settling velocity of hydrate-bearing quartz particles produced in the same batch falling in cold and warm water. Red symbols correspond to warm water, and blue symbols correspond to cold water. The upper and lower limits of the error line were obtained on the basis of the standard deviation of the ultimate settling velocity obtained in repeated falling experiments.

warm water, the bubbles produced from hydrate dissociation created more significant drag during particle motion.

When the water temperature $T_L = 343.15$ K, the bubble diameter was calculated to be $d_b = 2.8$ mm and it was determined that $d_b/\lambda_B \sim 5.59$. When the water temperature $T_L = 273.15$ K, the bubble diameter was calculated to be $d_b = 0.2$ mm and it was determined that $d_b/\lambda_B \sim 0.44$. The images of the hydrate-bearing quartz particles falling in cold and warm water obtained by the high-speed camera are shown in Figure 9. The bubbles from the dissociation in warm water were

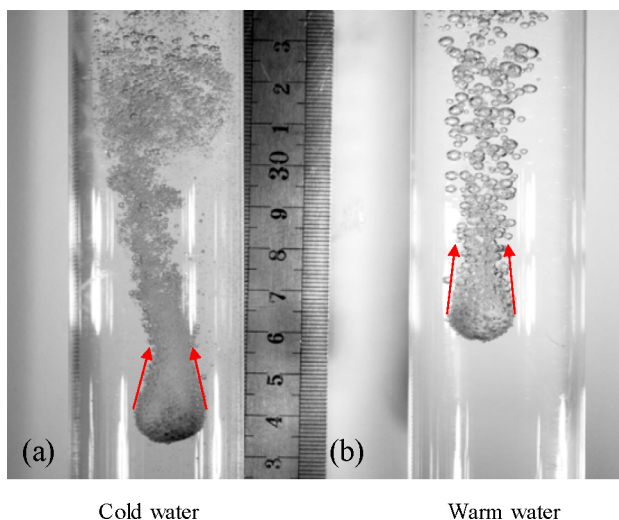


Figure 9. Dissociation of hydrate-bearing quartz particles in (a) cold water and (b) warm water. The red arrows indicate the trajectories of bubbles at the back ends of the particles.

significantly larger than those generated in cold water. The larger bubbles led to the earlier separation of the boundary layer, thus increasing the drag. The separation of the boundary layer could be determined using the trajectories of the bubbles at the back ends of the particles, as shown by the red arrow in Figure 9. The calculated diameters of the detaching bubble were consistent with the experimental results, which proved

that the calculation model was accurate. The values of the other physical parameters in the calculation process were consistent with those in Table 2. When the hydrate dissociation rate and the diameter of the bubbles on the particle surface were calculated under the condition of convective heat transfer, because the thermal conductivities of the dissociation and undissociated regions and the pore distribution of the particles could not be accurately measured, the above calculation results could only be used to qualitatively conclude that bubbles increased the particle motion drag. Thus, the influence of bubbles from the dissociation of hydrate-bearing particles on the particle motion requires further analysis. In addition, the dissociation experiments presented in this study were carried out under atmospheric pressure and did not take into account the effect of the pressure change on the bubble size and shape. Thus, the influence of bubbles from the dissociation of hydrate-bearing particles on the particle motion for the real deep ocean under high pressure requires further analysis.

5. CONCLUSION

An experimental study was carried out on the falling of hydrate-bearing particles in water. Parameters such as the settling velocity of the hydrate-bearing particles falling in the water and the bubble diameter were obtained. Furthermore, the influence of bubbles formed after hydrate dissociation on the settling characteristics and the drag coefficient of hydrate-bearing particles was analyzed.

When a particle fell in the water, the gas produced from the hydrate dissociation exited the pores of the particle, forming a large number of bubbles surrounding the particle. Driven by buoyancy, the bubbles at the front end of the particle slid upward along the particle surface and continued to move upward after falling off at a particular position at the back end of the particle. Within the Reynolds number range of this experiment, the drag coefficient variation range of the hydrate-bearing particles was $0.573 \leq C_D \leq 0.640$ and that of the non-hydrate particles was $0.481 \leq C_D \leq 0.560$. Mass transfer induced by hydrate dissociation disturbed the boundary layer on the particle surface, which caused the boundary layer to separate prematurely on both sides of the particle, thereby increasing the pressure drag of the particle motion. The reduction of the friction drag of the particle as a result of generated bubbles was insignificant in this experiment.

The effect of bubbles on the boundary layer disturbance could be measured using the ratio of the initial bubble diameter d_b formed when the gas exited the particle pores to the thickness λ_B of the viscous boundary layer. The detaching bubble diameter was closely related to the dissociation rate of the hydrate and the settling velocity of the particle. To explain the mechanism of the bubble effect on the particle motion, the heat transfer process and hydrate dissociation process of a single hydrate-bearing particle under water flow were studied in detail. The spatiotemporal evolution of the hydrate dissociation region expansion inside the particle was obtained. Furthermore, the maximum diameter d_b of bubbles detaching at the front end of the particle was obtained. At the same water temperature and settling velocity, although the hydrate saturation of the hydrate-bearing clay particles was different from that of the hydrate-bearing quartz particles, the maximum diameters of the bubbles detaching at the front ends of the particles were the same. Within the parameter ranges of this experiment, the diameters of the bubbles when detaching were

basically of the same order of magnitude as the thickness of the boundary layer, which indicated that the bubbles from the hydrate dissociation caused a significant disturbance to the boundary layer, thereby increasing the resistance of particle settling. When the experiment was carried out in the water at different temperatures, the bubbles from the dissociation in warm water were significantly larger than those generated in cold water. The larger bubbles led to the earlier separation of the boundary layer, which resulted in a smaller settling velocity when the particle was stable in warm water.

In conclusion, within the Reynolds number range of this experiment, the gas from the hydrate dissociation surrounded the particles, which increased the interaction forces between a particle and the water as the particle moved through the water. When the water was still, it increased the drag during the particle motion.

AUTHOR INFORMATION

Corresponding Author

Xuhui Zhang – Institute of Mechanics, Chinese Academy of Sciences, Beijing 100190, People's Republic of China; School of Engineering Science, University of Chinese Academy of Sciences, Beijing 100049, People's Republic of China; Southern Marine Science and Engineering Guangdong Laboratory (Guangzhou), Guangzhou 511458, People's Republic of China; orcid.org/0000-0001-9614-3679; Phone: +86-10-82544192; Email: zhangxuhui@imech.ac.cn

Authors

Peng Li – Institute of Mechanics, Chinese Academy of Sciences, Beijing 100190, People's Republic of China; orcid.org/0000-0002-1532-2999

Danning Liu – Institute of Mechanics, Chinese Academy of Sciences, Beijing 100190, People's Republic of China; School of Engineering Science, University of Chinese Academy of Sciences, Beijing 100049, People's Republic of China

Xiaobing Lu – Institute of Mechanics, Chinese Academy of Sciences, Beijing 100190, People's Republic of China; School of Engineering Science, University of Chinese Academy of Sciences, Beijing 100049, People's Republic of China

Complete contact information is available at:
<https://pubs.acs.org/10.1021/acs.energyfuels.0c03753>

Notes

The authors declare no competing financial interest.

ACKNOWLEDGMENTS

This study is supported by the National Natural Science Foundation of China (51639008 and 11872365), the Youth Innovation Promotion Association of Chinese Academy of Sciences (2017027), and the Key Special Project for Introduced Talents Team of Southern Marine Science and Engineering Guangdong Laboratory (Guangzhou, GML2019ZD0307).

REFERENCES

- (1) Tan, Z.; Pan, G.; Liu, P. Focus on the Development of Natural Gas Hydrate in China. *Sustainability* **2016**, *8* (6), 520.
- (2) Collett, T. S.; Lewis, R. E.; Winters, W. J.; Lee, M. W.; Rose, K. K.; Boswell, R. M. Downhole well log and core montages from the Mount Elbert Gas Hydrate Stratigraphic Test Well, Alaska North Slope. *Mar. Pet. Geol.* **2011**, *28* (2), 561–577.

- (3) Makogon, Y. E.; Holditch, S. A.; Makogon, T. Y. Russian field illustrates gas-hydrate production. *Oil Gas J.* **2005**, *103* (5), 43–47.

- (4) Zhang, X. H.; Lu, X. B.; Liu, L. L. Advances in natural gas hydrate recovery methods. *Prog. Geophys.* **2014**, *29* (2), 858–869 (in Chinese).

- (5) Li, C.; Huang, T.; Jia, W. A review of natural gas hydrates and its pipeline transportation technologies in deep water. *Kexue Tongbao (Chin. Ed.)* **2016**, *61* (22), 2449–2462.

- (6) Zhang, X.; Lu, X. A new exploitation method for gas hydrate in shallow stratum: Mechanical–thermal method. *Chin. J. Theor. Appl. Mech.* **2016**, *48* (5), 1238–1246 (in Chinese).

- (7) Wang, Z. Study on Annular Multiphase Flow Pattern Transition Mechanism Considering Gas Hydrate Phase Transition. Ph.D. Thesis, China University of Petroleum (East China), Qingdao, China, 2009 (in Chinese).

- (8) Wei, N.; Sun, W.; Meng, Y.; Zhou, S.; Li, G.; Guo, P.; Dong, K.; Li, Q. Sensitivity analysis of multiphase flow in annulus during drilling of marine natural gas hydrate reservoirs. *J. Nat. Gas Sci. Eng.* **2016**, *36*, 692–707.

- (9) Xu, H.; Kong, W.; Yang, F. Decomposition characteristics of natural gas hydrates in hydraulic lifting pipelines. *Nat. Gas Ind.* **2018**, *38* (7), 129–137 (in Chinese).

- (10) Tang, X. Pipeline Transportation Characteristics of Natural Gas Hydrate Slurry. Ph.D. Thesis, Southwest Petroleum University, Chengdu, China, 2018 (in Chinese).

- (11) Yin, Z.; Chong, Z. R.; Tan, H. K.; Linga, P. Review of gas hydrate dissociation kinetic models for energy recovery. *J. Nat. Gas Sci. Eng.* **2016**, *35*, 1362–1387.

- (12) Li, X.-S.; Xu, C.-G.; Zhang, Y.; Ruan, X.-K.; Li, G.; Wang, Y. Investigation into gas production from natural gas hydrate: A review. *Appl. Energy* **2016**, *172*, 286–322.

- (13) Falser, S.; Uchida, S.; Palmer, A. C.; Soga, K.; Tan, T. S. Increased Gas Production from Hydrates by Combining Depressurization with Heating of the Wellbore. *Energy Fuels* **2012**, *26* (10), 6259–6267.

- (14) Konno, Y.; Masuda, Y.; Hariguchi, Y.; Kurihara, M.; Ouchi, H. Key Factors for Depressurization-Induced Gas Production from Oceanic Methane Hydrates. *Energy Fuels* **2010**, *24* (3), 1736–1744.

- (15) Seol, Y.; Kneafsey, T. J. X-ray computed-tomography observations of water flow through anisotropic methane hydrate-bearing sand. *J. Pet. Sci. Eng.* **2009**, *66* (3–4), 121–132.

- (16) Li, B.; Li, X.-S.; Li, G.; Jia, J.-L.; Feng, J.-C. Measurements of Water Permeability in Unconsolidated Porous Media with Methane Hydrate Formation. *Energies* **2013**, *6* (7), 3622–3636.

- (17) Johnson, A.; Patil, S.; Dandekar, A. Experimental investigation of gas-water relative permeability for gas-hydrate-bearing sediments from the Mount Elbert Gas Hydrate Stratigraphic Test Well, Alaska North Slope. *Mar. Pet. Geol.* **2011**, *28* (2), 419–426.

- (18) Liu, X.; Flemings, P. B. Capillary effects on hydrate stability in marine sediments. *J. Geophys. Res.: Solid Earth* **2011**, *116*, B07102.

- (19) Li, P.; Zhang, X.; Lu, X. Dissociation equilibrium height and friction coefficient in pipeline transportation of gas hydrate-bearing sediment particles. *J. Nat. Gas Sci. Eng.* **2020**, *81*, 103470.

- (20) Murai, Y. Frictional drag reduction by bubble injection. *Exp. Fluids* **2014**, *55*, 1773.

- (21) Ceccio, S. L. Friction Drag Reduction of External Flows with Bubble and Gas Injection. *Annu. Rev. Fluid Mech.* **2010**, *42* (1), 183–203.

- (22) Vakarelski, I. U.; Marston, J. O.; Chan, D. Y.; Thoroddsen, S. T. Drag reduction by Leidenfrost vapor layers. *Phys. Rev. Lett.* **2011**, *106* (21), 214501.

- (23) Li, P.; Zhang, X.; Lu, X. Dissociation Behaviors of CO₂ Hydrate-Bearing Sediment Particle during Settling in Water. *Energies* **2018**, *11* (11), 2896.

- (24) Sloan, E. D., Jr. *Clathrate Hydrates of Natural Gases*; Marcel Dekker: New York, 1998.

- (25) Fukumoto, A.; Sean, W.-Y.; Sato, T.; Yamasaki, A.; Kiyono, F. Estimation of dissociation rate constant of CO₂ hydrate in water flow. *Greenhouse Gases: Sci. Technol.* **2015**, *5* (2), 169–179.

- (26) Vakarelski, I. U.; Chan, D. Y.; Thoroddsen, S. T. Drag Moderation by the Melting of an Ice Surface in Contact with Water. *Phys. Rev. Lett.* **2015**, *115* (4), 044501.
- (27) Sean, W.-Y.; Sato, T.; Yamasaki, A.; Kiyono, F. CFD and experimental study on methane hydrate dissociation Part I. Dissociation under water flow. *AIChE J.* **2007**, *53* (1), 262–274.
- (28) Zhang, X. H.; Lu, X. B.; Zheng, Z. M.; Zhang, L. M. Heat-Induced Evolution of Phase Transformations in Tetrahydrofuran Hydrate-Bearing Sediment. *J. Heat Transfer* **2014**, *136* (5), 052002.
- (29) Bansal, H.; Nikrityuk, P. A submodel for spherical particles undergoing phase change under the influence of convection. *Can. J. Chem. Eng.* **2017**, *95* (1), 150–156.
- (30) Yang, G. Q.; Luo, X.; Lau, R.; Fan, L. S. Bubble Formation in High-Pressure Liquid-Solid Suspensions with Plenum Pressure Fluctuation. *AIChE J.* **2000**, *46* (11), 2162–2174.